Nuclear astrophysics and electron beams

A. Schwenk[1]

Institut für Kernphysik, Technische Universität Darmstadt, 64289 Darmstadt, Germany and ExtreMe Matter Institute EMMI, GSI Helmholtzzentrum für Schwerionenforschung GmbH, 64291 Darmstadt, Germany

Abstract. Electron beams provide important probes and constraints for nuclear astrophysics. This is especially exciting at energies within the regime of chiral effective field theory (EFT), which provides a systematic expansion for nuclear forces and electroweak operators based on quantum chromodynamics. This talk discusses some recent highlights and future directions based on chiral EFT, including nuclear structure and reactions for astrophysics, the neutron skin and constraints for the properties of neutron-rich matter in neutron stars and core-collapse supernovae, and the dark matter response of nuclei.

CHIRAL EFFECTIVE FIELD THEORY

Chiral EFT is based on the symmetries of quantum chromodynamics (QCD) and is applicable at momentum scales of the order of the pion mass $Q \sim m_\pi$, where pions are included as explicit degrees of freedom and build up the long-range parts of strong interactions. In chiral EFT, nucleons interact via pion exchanges and shorter-range contact interactions [1, 2]. The resulting nuclear forces and consistent electroweak operators are organized in a systematic expansion in powers of Q/Λ_b, where $\Lambda_b \sim 500\,\mathrm{MeV}$ denotes the breakdown scale, leading to a typical expansion parameter $Q/\Lambda_b \sim 1/3$ for nuclei. As shown in Fig. 1, at a given order this includes contributions from one- or multi-pion exchanges and from contact interactions, with short-range couplings that are fit to data and thus capture all short-range effects relevant at low energies. The EFT enables one to estimate theoretical uncertainties and chiral EFT connects nuclear forces to the underlying theory through lattice QCD (see talk by W. Detmold) [3].

Chiral EFT opens up a systematic path to investigate many-body forces and their impact on few- and many-body systems [4]. This results from the consistency of NN and 3N interactions, which predicts the two-pion-exchange c_1, c_3, c_4 parts of 3N forces at N^{2}LO, leaving only two low-energy couplings c_D, c_E that encode pion interactions with short-range NN pairs and short-range three-body physics. The leading N^{2}LO 3N forces improve few-body scattering, but interesting open problems remain [5]. This makes the application of 3N and 4N forces at the next order (N^{3}LO) very exciting, in particular because they are predicted parameter-free with many new structures [1].

Because of gauge symmetries, the same EFT expansion is used to derive consistent electroweak operators. Therefore, the couplings in nuclear forces determine also electroweak processes. This provides an important consistency test and an exciting opportunity for electron beams. A prime example in chiral EFT are axial-vector weak currents, where pion interactions (due to the coupling to spin) contribute both to currents and to nuclear forces. This is already seen at leading order: The coupling g_A determines the axial one-body current and the one-pion-exchange potential. Two-body currents, also known as meson-exchange currents, enter at higher order, just like 3N forces. As shown in Fig. 1, the leading two-body axial-vector currents (at order Q^3) are due to long-range one-pion-exchange and short-range parts [6], with the same couplings c_3, c_4 and c_D of N^{2}LO 3N forces [7, 8]. Chiral EFT is essential for this connection, which can be viewed as the two-body analogue of the Goldberger-Treiman relation.

NUCLEAR STRUCTURE FRONTIERS

Recently, nuclear lattice simulations of light $N = Z$ nuclei, based on lattice chiral EFT interactions, have enabled first ab-initio calculations of the Hoyle state [9]. The triple-alpha structure and decay of this key state has been studied by electron scattering at the S-DALINAC [10], which provides precision tests in the chiral EFT regime.

[1] E-mail: schwenk@physik.tu-darmstadt.de

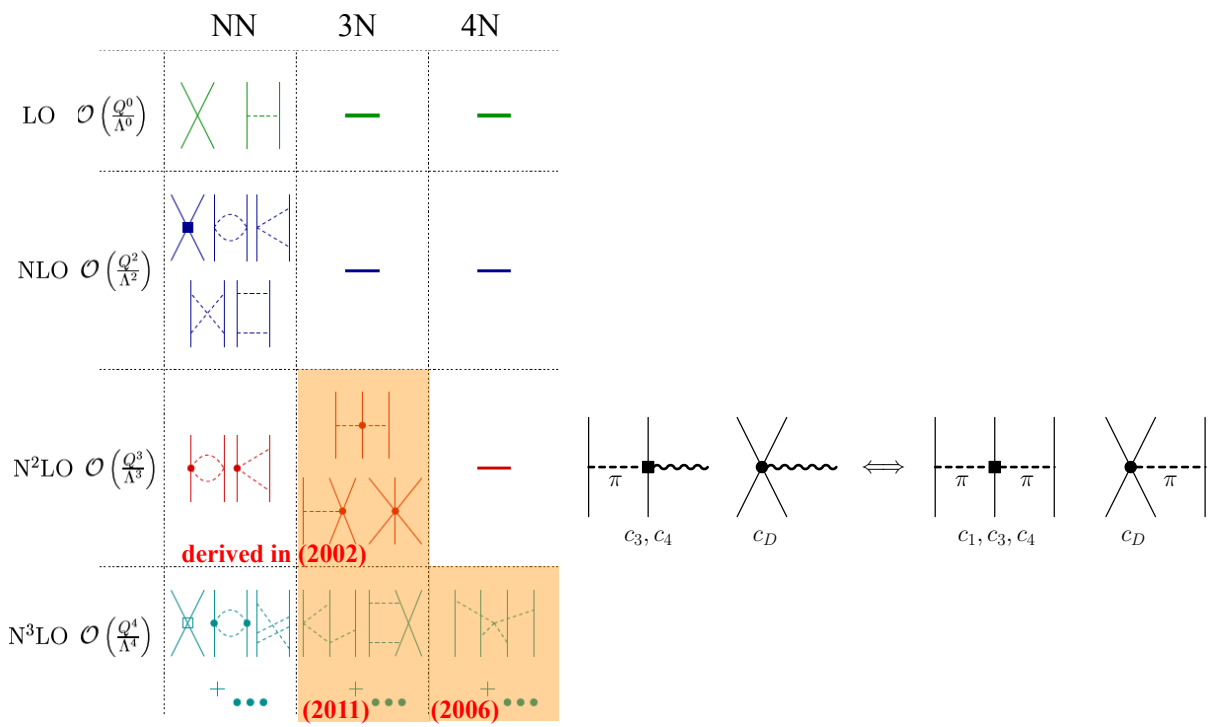

FIGURE 1. Chiral EFT for nuclear forces, where the different contributions at successive orders are shown diagrammatically [1, 2]. Many-body forces are highlighted in orange including the year they were derived. All N^{3}LO 3N and 4N forces are predicted parameter-free. On the right, as an example for electroweak operators, we show the leading two-body axial-vector weak currents that enter at order Q^3 and have the same couplings as in the leading 3N forces (indicated by the arrow) [6].

Three-nucleon forces are a frontier in the physics of nuclei and for nucleonic matter in stars. They play a key role in exotic nuclei, for shell structure and the evolution to the driplines. As shown in the left panels of Fig. 2, chiral 3N forces (fit only to ^{3}H and ^{4}He) lead to repulsive interactions between valence neutrons that change the location of the neutron dripline from ^{28}O (with NN forces only) to the experimentally observed ^{24}O [11, 12]. The position of the neutron dripline is driven by the location of the $d_{3/2}$ orbital, which remains unbound with 3N forces. This presents the first explanation of the oxygen anomaly based on nuclear forces. The 3N-force mechanism is dominated by the single-Δ contribution (see the shaded areas in Fig. 2) and was recently confirmed in large-space calculations [13, 14, 15].

In studies for calcium isotopes [16, 17, 18], it was shown that 3N forces are key to explain the $N = 28$ magic number, leading to a high 2^+ excitation energy and concentrated $B(M1)$ transition strength. Our NN+3N predictions for the masses of the neutron-rich calcium isotopes are shown in the right panel of Fig. 2. The predicted flat behavior of the two-neutron separation energy S_{2n} from ^{50}Ca to ^{52}Ca is in remarkable agreement with precision Penning-trap mass measurements of ^{51,52}Ca at TITAN/TRIUMF [19], which found ^{52}Ca to be 1.74 MeV more bound compared to the atomic mass evaluation. Recently, the ISOLTRAP collaboration at ISOLDE/CERN was able to advance the limits of precision mass measurements out to ^{54}Ca using a new multi-reflection time-of-flight mass spectrometer. The new ^{53,54}Ca masses are in excellent agreement with our predictions and unambiguously establish $N = 32$ as a shell closure (compare the pronounced decrease in S_{2n} after $N = 32$ to after $N = 28$), with a shell gap of almost 4 MeV [20]. Moreover, we have recently extended the NN+3N calculations to the mirror $Z = 8, 20$ isotone chains to study proton-rich exotic nuclei [21], which also test the understanding of isospin-symmetry-breaking nuclear forces.

NEUTRON SKINS AND NEUTRON STARS

For systems of only neutrons, the shorter-range c_D, c_E parts of 3N forces do not contribute because of the Pauli principle and the coupling of pions to spin [22]. Therefore, chiral EFT predicts all three-neutron and four-neutron forces to N^{3}LO. The same N^{2}LO 3N forces of the previous section are repulsive in neutron matter and dominate the

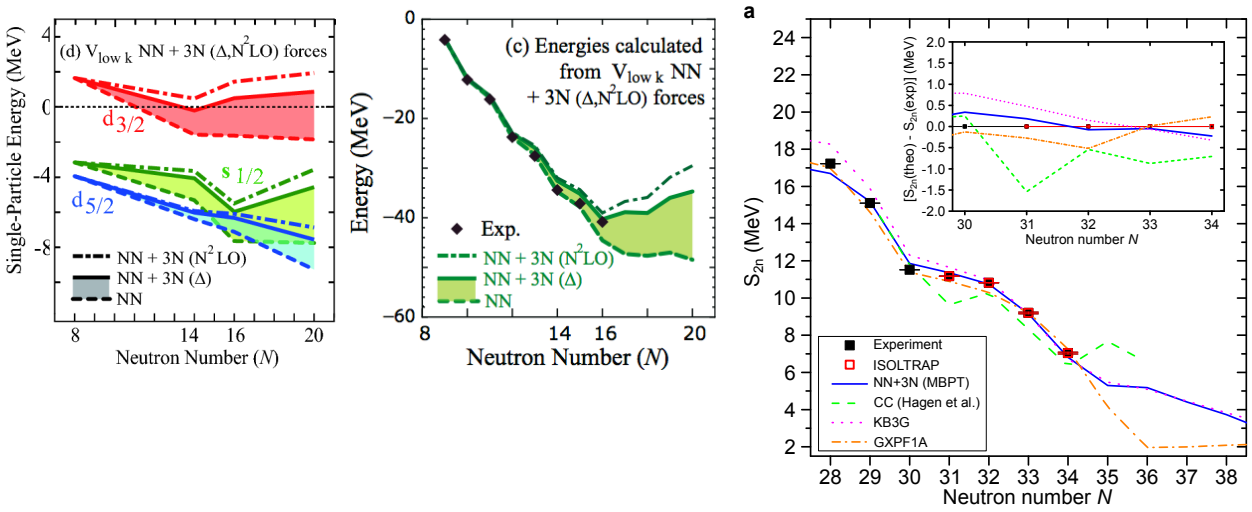

FIGURE 2. Left panel: Single-particle energies in the oxygen isotopes as a function of neutron number N. Results are shown based on NN forces only (RG-evolved to low-momentum interactions $V_{\mathrm{low}\,k}$) and with N^{2}LO 3N forces (NN+3N). Middle panel: Ground-state energies of the neutron-rich oxygen isotopes relative to ^{16}O, compared to the experimental energies of the bound isotopes $^{17-24}$O. In both panels, the changes due to the single-Δ contribution to 3N forces are highlighted by the shaded areas. For details see Ref. [11]. Right panel: Two-neutron separation energy S_{2n} of the neutron-rich calcium isotopes as a function of neutron number. Results first published in Nature [20]. The new ISOLTRAP energies are shown in red. Our predictions based on NN+3N forces are in excellent agreement with the S_{2n} values, with the flat behavior from ^{50}Ca to ^{52}Ca [19] and the pronounced decrease after the $N = 32$ shell closure [20] (see also the inset). For comparison, results are shown for large-space coupled-cluster (CC) calculations including 3N forces as density-dependent two-body interactions, and based on the phenomenological shell-model interactions KB3G and GXPF1A. For details see Ref. [20].

theoretical uncertainties of the neutron-matter energy [22]. As shown in the left panel of Fig. 3, the predicted energy range provides tight constraints for the symmetry energy S_v and its density derivative L. Neutron skins also probe the neutron-matter energy and pressure. Our results predict a neutron skin thickness of 0.17 ± 0.03 fm for ^{208}Pb [23], in excellent agreement with a recent determination of $0.156^{+0.025}_{-0.021}$ fm from the complete electric dipole response [26]. In addition, this can be tested with future determinations of the neutron skin of ^{208}Pb and ^{48}Ca using parity-violating electron scattering at JLab [27]. See also the talks by J. Piekarewicz, M. Dalton, and C. Sfienti.

To study the predicted 3N and 4N forces, we have performed the first complete N^{3}LO calculation of neutron matter including NN, 3N and 4N interactions [28, 29]. The resulting energy is shown in the right panel of Fig. 3, where the uncertainty band is dominated by the uncertainty in the c_i couplings of the N^{2}LO 3N forces. The energy range is also consistent with the RG-evolved results of Ref. [22]. Moreover, first Quantum Monte Carlo calculations with chiral EFT interactions are providing nonperturbative benchmarks for neutron matter at nuclear densities [30], and there are also calculations of neutron matter using in-medium chiral perturbation theory approaches [31, 32].

The neutron-matter calculations based on chiral EFT interactions constrain the properties of neutron-rich matter below nuclear densities to a much higher degree than is reflected in current neutron star modeling [23] and in equations of state for core-collapse supernova simulations [29]. The constraints for the pressure of neutron-star matter are shown in the left panel of Fig. 4 and rule out many model equations of state [23, 24]. Combined with the heaviest observed $2M_\odot$ neutron stars [33, 34] and general extensions to high densities, our N^{3}LO neutron-matter results constrain the mass-radius of neutron stars to the red region in the right panel of Fig. 4, e.g., the radius of a typical $1.4M_\odot$ star to $R = 9.7 - 13.9$ km [24, 29] (the same relative uncertainty as for the neutron skin). The predicted radius range is due, in about equal amounts, to the uncertainty in 3N forces and to the extrapolation to high densities. The physics of 3N forces therefore connects neutron-rich nuclei with neutron stars. The radius range is also consistent with astrophysical extractions obtained from modeling X-ray burst sources (see, e.g., Ref. [35]). Finally, the neutron-matter constraints have recently been explored for the gravitational wave signal in neutron-star mergers [36].

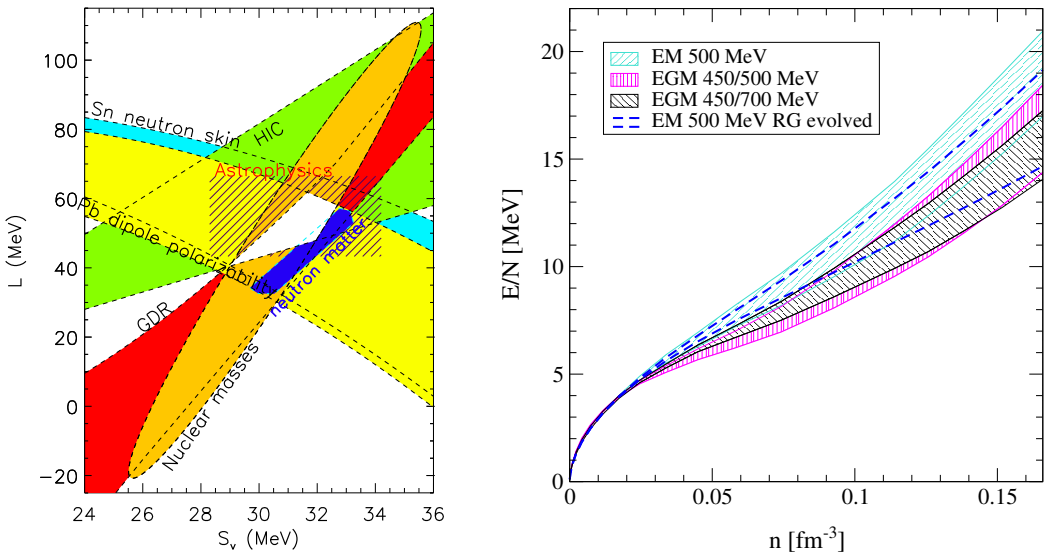

FIGURE 3. Left panel: Constraints for the symmetry energy S_v and its density derivative L. The blue region shows our neutron-matter constraints [24], in comparison to bands from different empirical extractions [25]. The white area gives the overlap region of the different empirical ranges. For details see Ref. [24]. Right panel: Neutron-matter energy per particle E/N as a function of density n including NN, 3N, and 4N forces at N^{3}LO. The three overlapping bands are based on different NN potentials (see legend) and include uncertainty estimates due to the many-body calculation, the low-energy c_i couplings in 3N forces (which dominate the uncertainty), and by varying the 3N/4N cutoffs. For comparison, we show the results for the RG-evolved NN EM 500 MeV potential including only N^{2}LO 3N forces from Ref. [22]. For details see Ref. [28].

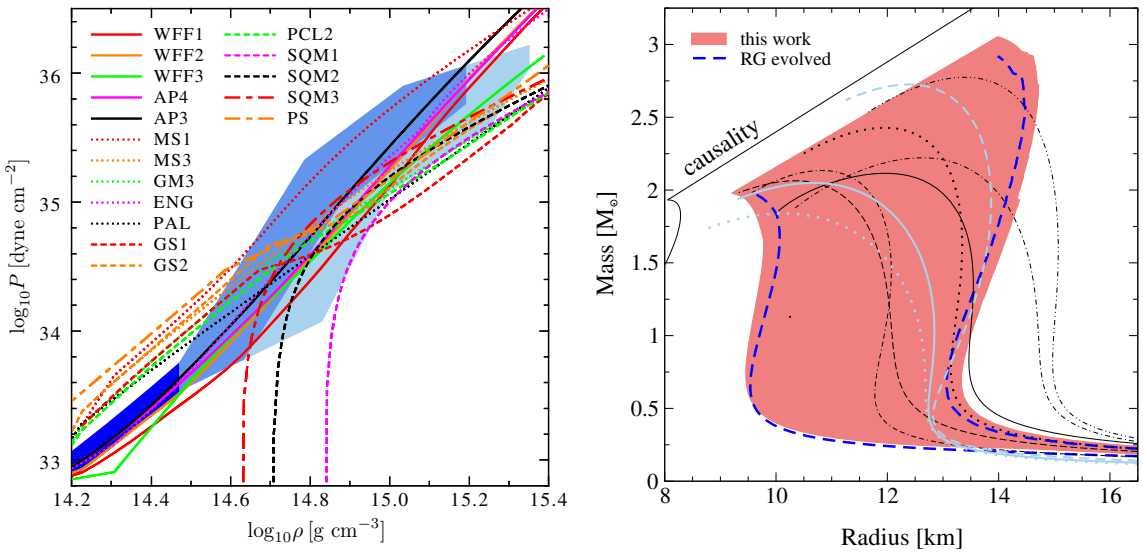

FIGURE 4. Left panel: Constraints for the pressure P of neutron-star matter as a function of mass density ρ compared to equations of state commonly used to model neutron stars. The blue band at low densities represents the pressure predicted by our neutron matter calculations and incorporating beta equilibrium. The bands at high densities are the envelope of general polytropic extensions that are causal and support a neutron star of mass $1.97\,M_\odot$ (lighter blue) and $2.4\,M_\odot$ (darker blue). For details see Ref. [24]. Right panel: Constraints on the mass-radius diagram of neutron stars based on our N^{3}LO neutron-matter results and following Ref. [24] for the extension to neutron-star matter and to high densities (red band), in comparison to the constraints based on RG-evolved interactions (thick dashed blue lines, based on the $1.97\,M_\odot$ band of the left panel). We also show the mass-radius relations obtained from equations of state for core-collapse supernova simulations. For details see Ref. [29].

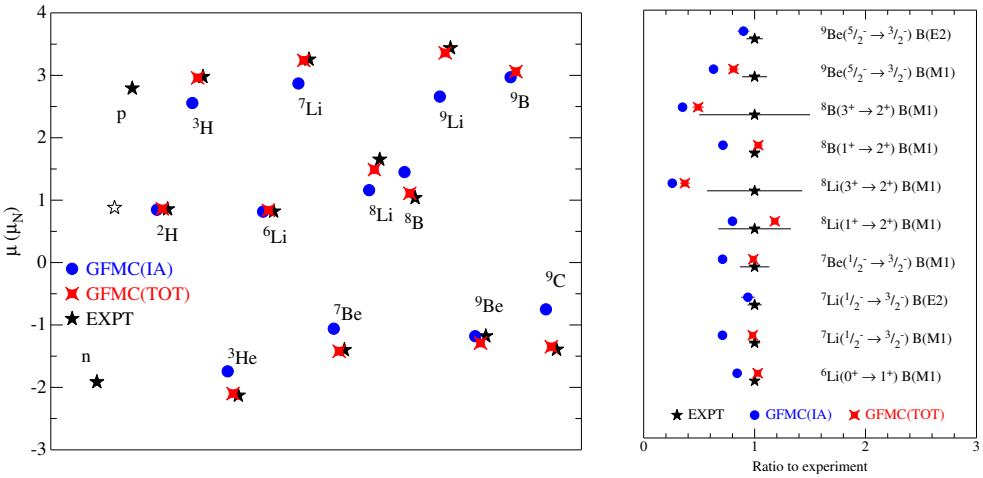

FIGURE 5. Magnetic moments in nuclear magnetons (left panel) and ratio theory to experiment for $B(M1)$ and $B(E2)$ transition strengths (right panel) in $A \leqslant 9$ nuclei. Results are based on GFMC calculations with phenomenological NN and 3N forces, including one-body currents (IA) and two-body currents to N^{3}LO (TOT) based on chiral EFT, in comparison with experiment. Figure from Ref. [39]. Copyright (2013) by The American Physical Society.

ELECTROWEAK INTERACTIONS

Chiral EFT predicts consistent one- and two-body electroweak currents. For electromagnetic reactions, two-body currents have been derived recently and applied to few-nucleon systems [37, 38] (see talk by H. Griesshammer). A highlight are the GFMC calculations of magnetic moments and electromagnetic transitions in light nuclei [39] shown in Fig. 5. The results demonstrate that two-body currents provide significant contributions to electromagnetic processes, especially for larger A. There are also interesting sensitivities to 3N forces in electron scattering off light nuclei [40].

While chiral EFT currents have been studied in light nuclei, they were only recently explored in medium-mass nuclei with a focus on axial-vector weak currents [41]. Compared to light nuclei, the contributions of two-body currents are amplified in medium-mass nuclei because of the larger nucleon momenta. Using a normal-ordering approximation for two-body currents to create a density-dependent operator [42], it was shown that the leading two-body axial currents of Fig. 1 contribute mainly to the Gamow-Teller operator and that the 3N couplings predict a quenching of low-momentum-transfer Gamow-Teller transitions, dominated by the single-Δ contribution [41]. This demonstrates that chiral two-body currents naturally contribute to the quenching of Gamow-Teller transitions. A reduction of g_A in the currents is also expected considering chiral 3N forces as density-dependent two-body interactions [43].

Neutrinoless double-beta decay presents a fundamental test of the nature of the neutrino, of lepton number, and the neutrino mass scale and hierarchy. A key input for the ongoing and planned experimental searches are the nuclear matrix elements that incorporate the structure of the parent and daughter nuclei and of the decay mechanism. Compared to standard beta decays, neutrinoless double-beta decay probes different momentum transfers $Q \sim 100\,\mathrm{MeV} \sim m_\pi$ [44]. Therefore, the impact of two-body currents and renormalization effects can differ from the suppression of g_A in medium-mass nuclei. Chiral EFT predicts the momentum-transfer dependence of two-body currents, which varies on the order of the pion mass due to the one-pion-exchange part in the currents in Fig. 1. The first calculation of the neutrinoless double-beta decay operator based on chiral EFT currents at successive order is shown in Fig. 6 [41]. This demonstrates that the contributions from two-body currents are significant and should be included in all calculations. An interesting question is how electron beams can test and constrain the operator and nuclear structure involved.

A clever idea to study nuclear reactions for astrophysics is to use electrons to simulate neutrino-nucleus scattering for supernovae and nucleosynthesis [45]. The relevant inelastic cross sections are mainly determined by the Gamow-Teller response, which can be constrained by (e,e') $M1$ data, provided the orbital contribution is small or can be removed. This has been realized with precision $M1$ data at the S-DALINAC [45]. Recently, there are exciting developments for nucleosynthesis in core-collapse supernovae due to observations of ultra metal-poor stars that probe the early chemical evolution. Simulations of the neutrino-driven wind in supernovae can reproduce the lighter r-process Sr to Ag abundances as observed in ultra metal-poor stars, both for neutron- or proton-rich wind conditions [46]. So the reactions for making Sr to Ag are closer to stability and thus more accessible.

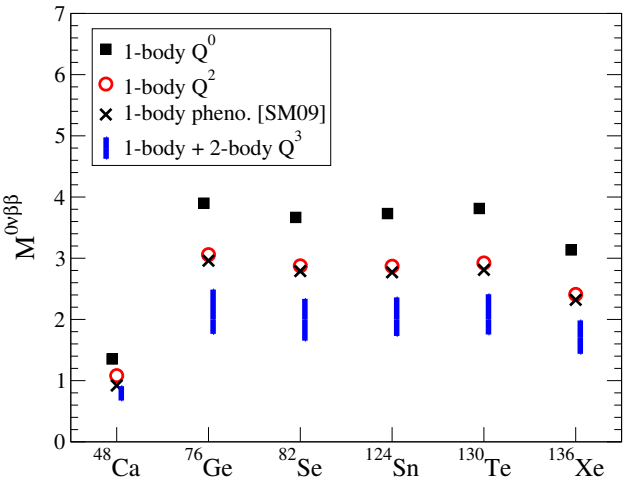

FIGURE 6. Nuclear matrix elements $M^{0\nu\beta\beta}$ for neutrino-less double-beta decay of different nuclei. Results are shown based on chiral EFT currents at successive orders, including one-body currents at orders Q^0 and Q^2, and the predicted long-range parts of two-body currents at order Q^3 ([41]; for details and a discussion of the short-range contributions, see this reference). For comparison, we also show shell-model results (SM09) of Ref. [44] based on phenomenological one-body currents only.

DARK MATTER RESPONSE OF NUCLEI

Direct dark matter detection needs structure factors for elastic WIMP-nucleus scattering as input, which is particularly sensitive to nuclear structure for spin-dependent WIMP-nucleon interactions. The relevant momentum transfers p involved in WIMP scattering off nuclei are of the order of the pion mass, so that this is a prime regime for chiral EFT. We have developed the spin-dependent WIMP-nucleon currents in chiral EFT including the long-range two-body currents, which are predicted [47, 48] (see Ref. [49] for other possible WIMP-nucleon interactions and Ref. [50] for the application of chiral EFT to the spin-independent case). The spin-dependent WIMP-nucleon currents are an isospin rotation of the axial-vector weak currents shown in Fig. 1.

We have performed state-of-the-art large-scale shell-model calculations of the structure factors for spin-dependent WIMP scattering off ^{129,131}Xe, ^{127}I, ^{73}Ge, ^{19}F, ^{23}Na ,^{27}Al, and ^{29}Si, which covers the non-zero-spin nuclei relevant to direct dark matter detection [47, 48]. For recent work on the signatures of dark matter scattering inelastically off nuclei see Ref. [51]. Our calculations are in the largest valence spaces with nuclear interactions that have been used in nuclear structure and decay studies in these mass regions and yield a good spectroscopic description, as shown for ^{129}Xe and ^{131}Xe in the left panel of Fig. 7. Our results for the structure factors for spin-dependent WIMP scattering include theoretical error bands due to the nuclear uncertainties of WIMP currents in nuclei. The structure factors for ^{129}Xe and ^{131}Xe in the right panel of Fig. 7 show that for these odd-neutron nuclei, two-body currents lead to a significant increase of the "proton-only" structure factors, which follow the "neutron-only" ones at low momentum transfers. This is because of strong interactions between nucleons through two-body currents that allow the odd species carrying most of the spin to contribute (see Ref. [48] for a detailed discussion). In fact, with two-body currents, both "proton/neutron-only" structure factors are determined by the spin distribution of the odd species. Our results for ^{129}Xe and ^{131}Xe were recently used as the benchmark calculation by the XENON100 collaboration, which provides the best limits for spin-dependent WIMP-neutron couplings [52]. Also here an interesting question is whether it is possible to simulate/constrain the dark matter response of nuclei with electron beams.

ACKNOWLEDGMENTS

I would like to thank A. Bauswein, K. Blaum, J. Dilling, B. Friman, A. T. Gallant, D. Gazit, A. Gezerlis, K. Hebeler, J. D. Holt, H.-T. Janka, P. Klos, T. Krüger, J. M. Lattimer, J. Menéndez, C. J. Pethick, T. Otsuka, L. Schweikhard, J. Simonis, T. Suzuki, I. Tews, and F. Wienholtz, who contributed to the results presented in this talk, and the organizers of this excellent workshop. This work was supported by ARCHES, the BMBF under Contract No. 06DA70471, the DFG through Grant SFB 634, the ERC Grant No. 307986 STRONGINT, and the Helmholtz Alliance HA216/EMMI.

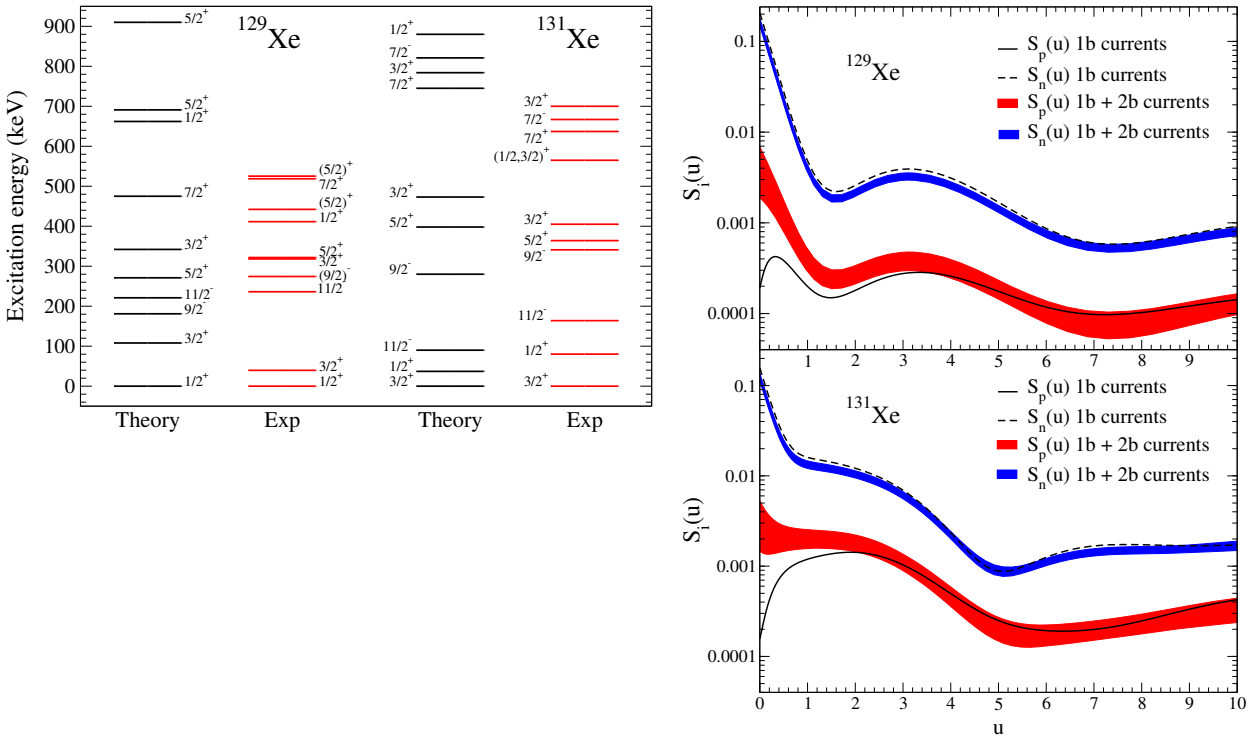

FIGURE 7. Left panel: Comparison of calculated spectra of ^{129}Xe and ^{131}Xe with experiment. For details see Ref. [47]. Right panel: Structure factors for spin-dependent WIMP scattering off ^{129}Xe (top) and ^{131}Xe (bottom). Results are shown for WIMP-"proton-only" $S_p(u)$ (solid lines) and "neutron-only" couplings $S_n(u)$ (dashed lines) as a function of $u = p^2b^2/2$, with momentum transfer p and harmonic-oscillator length b, at the one-body (1b) current level and including two-body (2b) currents. The estimated theoretical uncertainty in WIMP-nucleon currents is given by the red ($S_p(u)$) and blue ($S_n(u)$) bands. For details see Refs. [47, 48].

REFERENCES

1. E. Epelbaum, H.-W. Hammer, and U.-G. Meißner, *Rev. Mod. Phys.* **81**, 1773 (2009).
2. R. Machleidt and D. R. Entem, *Phys. Rept.* **503**, 1 (2011).
3. S. R. Beane, W. Detmold, K. Orginos, and M. J. Savage, *Prog. Part. Nucl. Phys.* **66**, 1 (2011).
4. H.-W. Hammer, A. Nogga, and A. Schwenk, *Rev. Mod. Phys.* **85**, 197 (2013).
5. N. Kalantar-Nayestanaki, E. Epelbaum, J. G. Messchendorp, and A. Nogga, *Rept. Prog. Phys.* **75**, 016301 (2012).
6. T. S. Park *et al.*, *Phys. Rev. C* **67**, 055206 (2003).
7. A. Gårdestig and D. R. Phillips, *Phys. Rev. Lett.* **96**, 232301 (2006).
8. D. Gazit, S. Quaglioni, and P. Navrátil, *Phys. Rev. Lett.* **103**, 102502 (2009).
9. E. Epelbaum, H. Krebs, D. Lee, and U.-G. Meißner, *Phys. Rev. Lett.* **106**, 192501 (2011); E. Epelbaum, H. Krebs, T. A. Lahde, D. Lee, and U.-G. Meißner, *Phys. Rev. Lett.* **109**, 252501 (2012).
10. M. Chernykh, H. Feldmeier, T. Neff, P. von Neumann-Cosel, and A. Richter, *Phys. Rev. Lett.* **98**, 032501 (2007); *ibid.* **105**, 022501 (2010).
11. T. Otsuka, T. Suzuki, J. D. Holt, A. Schwenk, and Y. Akaishi, *Phys. Rev. Lett.* **105**, 032501 (2010).
12. J. D. Holt, J. Menéndez, and A. Schwenk, *Eur. Phys. J. A* **49**, 39 (2013).
13. G. Hagen, M. Hjorth-Jensen, G. R. Jansen, R. Machleidt, and T. Papenbrock, *Phys. Rev. Lett.* **108**, 242501 (2012).
14. H. Hergert, S. Binder, A. Calci, J. Langhammer, and R. Roth, *Phys. Rev. Lett.* **110**, 242501 (2013).
15. A. Cipollone, C. Barbieri, and P. Navrátil, *Phys. Rev. Lett.* **111**, 062501 (2013).
16. J. D. Holt, T. Otsuka, A. Schwenk, and T. Suzuki, *J. Phys. G* **39**, 085111 (2012).
17. G. Hagen, M. Hjorth-Jensen, G. R. Jansen, R. Machleidt, and T. Papenbrock, *Phys. Rev. Lett.* **109**, 032502 (2012).
18. J. D. Holt, J. Menéndez, and A. Schwenk, *J. Phys. G* **40**, 075105 (2013).
19. A. T. Gallant *et al.*, *Phys. Rev. Lett.* **109**, 032506 (2012).
20. F. Wienholtz *et al.*, *Nature* **498**, 346 (2013).
21. J. D. Holt, J. Menéndez, and A. Schwenk, *Phys. Rev. Lett.* **110**, 022502 (2013).
22. K. Hebeler and A. Schwenk, *Phys. Rev. C* **82**, 014314 (2010).
23. K. Hebeler, J. M. Lattimer, C. J. Pethick, and A. Schwenk, *Phys. Rev. Lett.* **105**, 161102 (2010).

24. K. Hebeler, J. M. Lattimer, C. J. Pethick, and A. Schwenk, *Astrophys. J.* **773**, 11 (2013).
25. J. M. Lattimer and Y. Lim, *Astrophys. J.* **771**, 51 (2013).
26. A. Tamii *et al.*, *Phys. Rev. Lett.* **107**, 062502 (2011).
27. S. Abrahamyan *et al.*, *Phys. Rev. Lett.* **108**, 112502 (2012).
28. I. Tews, T. Krüger, K. Hebeler, and A. Schwenk, *Phys. Rev. Lett.* **110**, 032504 (2013).
29. T. Krüger, I. Tews, K. Hebeler, and A. Schwenk, *Phys. Rev. C* **88**, 025802 (2013).
30. A. Gezerlis, I. Tews, E. Epelbaum, S. Gandolfi, K. Hebeler, A. Nogga, and A. Schwenk, *Phys. Rev. Lett.* **111**, 032501 (2013).
31. J. W. Holt, N. Kaiser, and W. Weise, arXiv:1304.6350.
32. A. Lacour, J. A. Oller, and U.-G. Meißner, *Annals Phys.* **326**, 241 (2011).
33. P. B. Demorest, T. Pennucci, S. M. Ransom, M. S. E. Roberts, and J. W. T. Hessels, *Nature* **467**, 1081 (2010).
34. J. Antoniadis *et al.*, *Science* **340**, 448 (2013).
35. A. W. Steiner, J. M. Lattimer, and E. F. Brown, *Astrophys. J.* **722**, 33 (2010).
36. A. Bauswein and H.-T. .Janka, *Phys. Rev. Lett.* **108**, 011101 (2012); A. Bauswein, H.-T. Janka, K. Hebeler, and A. Schwenk, *Phys. Rev. D* **86**, 063001 (2012).
37. S. Kolling, E. Epelbaum, H. Krebs, and U.-G. Meißner, *Phys. Rev. C* **84**, 054008 (2011).
38. M. Piarulli, L. Girlanda, L. E. Marcucci, S. Pastore, R. Schiavilla, and M. Viviani, *Phys. Rev. C* **87**, 014006 (2013).
39. S. Pastore, S. C. Pieper, R. Schiavilla, and R. B. Wiringa, *Phys. Rev. C* **87**, 035503 (2013).
40. S. Bacca, N. Barnea, W. Leidemann, and G. Orlandini, *Phys. Rev. Lett.* **102**, 162501 (2009); *Phys. Rev. C* **80**, 064001 (2009).
41. J. Menéndez, D. Gazit, and A. Schwenk, *Phys. Rev. Lett.* **107**, 062501 (2011).
42. B. Friman and A. Schwenk, in *From Nuclei to Stars: Festschrift in Honor of Gerald E. Brown*, Ed. S. Lee (World Scientific, 2011) arXiv:1101.4858.
43. J. W. Holt, N. Kaiser, and W. Weise, *Phys. Rev. C* **81**, 024002 (2010).
44. J. Menéndez, A. Poves, E. Caurier, and F. Nowacki, *Nucl. Phys. A* **818**, 139 (2009).
45. K. Langanke, G. Martínez-Pinedo, P. von Neumann-Cosel, and A. Richter, *Phys. Rev. Lett.* **93**, 202501 (2004).
46. A. Arcones and F. Montes, *Astrophys. J.* **731**, 5 (2011).
47. J. Menéndez, D. Gazit, and A. Schwenk, *Phys. Rev. D* **86**, 103511 (2012).
48. P. Klos, J. Menéndez, D. Gazit, and A. Schwenk, arXiv:1304.7684.
49. A. L. Fitzpatrick, W. C. Haxton, E. Katz, N. Lubbers, and Y. Xu, *JCAP* **1302**, 004 (2013).
50. V. Cirigliano, M. L. Graesser, and G. Ovanesyan, *JHEP* **1210**, 025 (2012).
51. L. Baudis, G. Kessler, P. Klos, R. F. Lang, J. Menéndez, S. Reichard, and A. Schwenk, arXiv:1309.0825.
52. E. Aprile *et al.* (XENON100 Collaboration), *Phys. Rev. Lett.* **111**, 021301 (2013).